



Willoughby, R., Cotterell, M., Lin, H., Orr-Ewing, A., & Reid, J. (2017). Measurements of the imaginary component of the refractive index of weakly absorbing single aerosol particles. *Journal of Physical Chemistry A*, 121(30), 5700-5710. <https://doi.org/10.1021/acs.jpca.7b05418>

Peer reviewed version

Link to published version (if available):
[10.1021/acs.jpca.7b05418](https://doi.org/10.1021/acs.jpca.7b05418)

[Link to publication record in Explore Bristol Research](#)
PDF-document

This is the author accepted manuscript (AAM). The final published version (version of record) is available online via ACS Publishing at <http://pubs.acs.org/doi/abs/10.1021/acs.jpca.7b05418>. Please refer to any applicable terms of use of the publisher.

University of Bristol - Explore Bristol Research

General rights

This document is made available in accordance with publisher policies. Please cite only the published version using the reference above. Full terms of use are available: <http://www.bristol.ac.uk/pure/user-guides/explore-bristol-research/ebr-terms/>

1 **Measurements of the Imaginary Component of the Refractive Index of**
2 **Weakly Absorbing Single Aerosol Particles**

3 Rose E. Willoughby¹, Michael I. Cotterell^{1,2,3}, Hongze Lin⁴,

4 Andrew J. Orr-Ewing¹ and Jonathan P. Reid^{1*}

5 ¹School of Chemistry, University of Bristol, Cantock's Close, Bristol BS8 1TS, UK

6 ²College for Engineering, Mathematics and Physical Sciences, University of Exeter, EX4 4QF, UK

7 ³Aerosol Observation Based Research, Met Office, EX1 3PB, UK

8 ⁴ College of Optical Science and Engineering, Zhejiang University, Hangzhou 310058, China

9
10 *Author for correspondence: j.p.reid@bristol.ac.uk

11
12 **Abstract**

13 The interaction of atmospheric aerosols with radiation remains a significant source of uncertainty
14 in modelling radiative forcing. Laboratory measurements of the microphysical properties of
15 atmospherically relevant particles is one approach to reduce this uncertainty. We report a new
16 method to investigate light absorption by a single aerosol particle, inferring changes in the
17 imaginary part of the refractive index with change in environmental conditions (e.g. relative
18 humidity) and inferring the size dependence of the optical extinction cross-section. More
19 specifically, we present measurements of the response of single aerosol particles to near infrared
20 (NIR) laser induced heating at a wavelength 1520 nm. Particles were composed of aqueous NaCl
21 or (NH₄)₂SO₄ and were studied over ranges in relative humidity (40 - 85%), particle radius (1 –
22 2.2 μm) and NIR laser power. The ensuing size change and real component of the refractive index
23 were extracted from measurements of the angular variation in elastically scattered light. From the
24 heating-induced size change at varying NIR beam intensities, we retrieved the change in the
25 imaginary component of the refractive index. In addition, cavity ring-down spectroscopy
26 measurements monitored the change in extinction cross-section with modulation of the heating
27 laser power.

29 Introduction

30 The ability of aerosols to scatter and absorb solar and terrestrial radiation is governed by particle
31 size, morphology, mixing state and refractive index (RI). The single scattering albedo (SSA) is an
32 important optical property in determining the net influence of aerosols on the Earth's radiative
33 balance. The SSA is the ratio of the scattering (σ_{sca}) and total extinction (σ_{ext}) cross sections of a
34 particle, with accurate characterizations of these optical quantities of utmost importance for
35 improving the representation of aerosol in climate models.¹ To measure the SSA of aerosol
36 particles, at least two of the three light attenuation coefficients (scattering, absorption and
37 extinction) must be quantified. Providing aerosol particles are homogeneous and spherical, the
38 optical attenuation coefficients and SSA can be calculated using Mie theory for a particle of
39 arbitrary size, if the complex refractive index is known. The complex RI, m , consists of a real
40 component (n) that influences the extent of light scattering and an imaginary component (k) that
41 determines the magnitude of light absorption. For aerosol particles of diameter 150 nm with n
42 equivalent to that of ammonium sulfate, Zarzana and co-workers calculated that an uncertainty of
43 ± 0.01 in k translates into to an uncertainty of $\pm 20\%$ in radiative forcing.² Moreover, a reduction
44 in k from 0.05 to 0 for secondary organic aerosols (SOA) has been shown to decrease the estimated
45 cooling effect of an aerosol by a factor of 3.³ These studies emphasize the importance of measuring
46 accurate refractive indices to improve the quantification of the direct contribution by aerosols to
47 radiative forcing.

48 Aerosol cavity ring-down spectroscopy (A-CRDS) and cavity enhanced extinction spectroscopy
49 (CEES) have been used extensively to measure the extinction coefficients of ensemble aerosol.⁴⁻⁹
50 These measurements of aerosol extinction have been used to retrieve the complex refractive index
51 of a range of aerosol species, such as secondary organic aerosol, inorganic species and mineral
52 dust.^{6,10-14} Typical uncertainties for A-CRDS for the real component of the RI are $n \pm 0.02$.⁹ The
53 size distributions and number concentrations of the ensemble of aerosols are selected prior to
54 extinction measurements, commonly with a differential mobility analyzer, the use of which
55 introduces $\sim 10\%$ uncertainty into the extinction measurements.¹⁵⁻¹⁷ Zarzana *et al.* showed that the
56 RIs retrieved from extinction-only measurements are too inaccurate to merit use in radiative
57 forcing calculations.² The same study showed that when more than one attenuation coefficient was

58 measured, the greater accuracy in the retrieved complex RI significantly improved estimates of
59 radiative forcing.²

60 Many current research methods combine measurements of extinction, scattering and absorption to
61 retrieve superior precision in aerosol refractive index.^{15,18,19} Aerosol extinction measurements
62 from CRDS have been combined with scattering measurements from nephelometry to allow the
63 aerosol absorption to be derived from the difference between the two measurements,^{20,21} resulting
64 in SSA measurements with an expected associated error of < 2.9%.¹⁵ Photoacoustic spectroscopy
65 (PAS) has been used to measure aerosol absorption,²² with the upper limit of instrument precision
66 stated as ~ 6%.¹⁸ Combining PAS with CRDS has enabled the complex refractive index of SOA
67 to be studied, with typical uncertainties in $n < \pm 0.006$ and $k < \pm 0.002$.²³ Recent measurements by
68 Bluvshstein and co-authors combined extinction, scattering and absorption measurements from
69 CEES, PAS, CRDS and nephelometry to obtain the SSA of brown carbon proxies from 300-650
70 nm.²⁴

71 Laboratory studies of single aerosol particles allow the fundamental aerosol microphysical
72 properties to be deduced with enhanced precision. The precise size (to nm accuracy) and
73 microphysical properties of a single particle with a known composition can be measured, thus
74 eliminating additional uncertainty associated with ensemble measurements of aerosol size and
75 number distributions.⁹ The optical properties of particles of known composition can be probed
76 with high precision, enabling predictive mixing rules to be compared and assessed.²⁵ Single aerosol
77 particles have been studied with a number of different experimental techniques. For example, PAS
78 of an optically trapped single aerosol particle was recently proven to be a potentially powerful tool
79 for elucidating photochemical reactions that occur in the atmosphere.²⁶ Single particle
80 nephelometry has been developed to measure the complex refractive index and distinguish
81 between spherical and non-spherical particles.²⁷ The absorbing properties of single aerosol
82 particles trapped with aerosol optical tweezers have been retrieved from whispering gallery modes
83 observed by Raman spectroscopy.²⁸ This technique provided the real refractive index to a precision
84 of ± 0.0012 (better than ± 0.11 %) and, in a limited number of studies, the technique has been
85 shown to be sufficiently sensitive to allow the determination of imaginary refractive indices as
86 small as 1×10^{-8} .²⁸

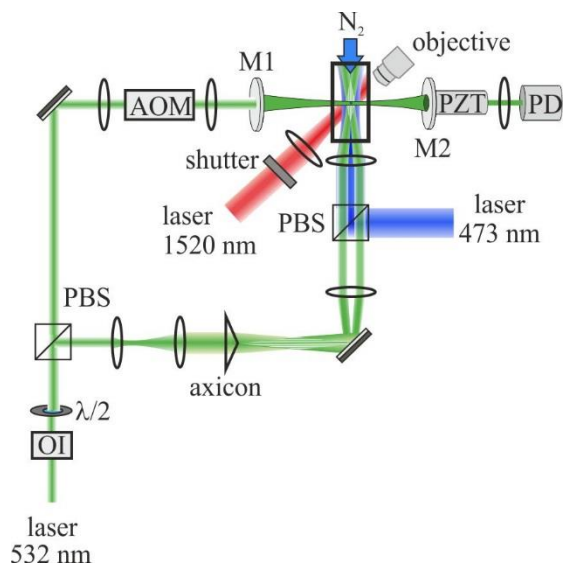
87 Within the atmosphere, aerosols experience varying environmental conditions, such as changes to
88 relative humidity (RH) which alter the composition of a particle and consequently the
89 physiochemical properties that affect their radiative forcing. It is therefore imperative to study the
90 optical properties of aerosol particles at varying humidities. We have developed a single particle
91 cavity ring-down spectroscopy (SP-CRDS) instrument with demonstrated high precision in the
92 retrieved real component of the refractive index, with a typical uncertainty of ± 0.003 in n .²⁹ We
93 recently reported a parameterization of the real RI in terms of both RH and wavelength for a
94 variety of inorganic aerosol components.²⁹ The current work presents a novel strategy to measure
95 simultaneously the extinction and absorption of a single aerosol particle by introducing an
96 additional heating laser beam into our SP-CRDS instrument. This heating laser beam can be used
97 to induce a size change from which the change in k (Δk) can be determined. In many ways the
98 underlying process is similar to the approach used in PAS instruments, except here we report
99 changes to the particle size directly, rather than probe the pressure wave that propagates following
100 heat and mass transfer from an evaporating heated aerosol particle. Here, we present the retrieval
101 of the change in k from single, weakly absorbing aerosol particles at a number of discrete
102 humidities (from ~ 40 - 85% RH). We model the change in particle size, temperature and vapor
103 pressure when a particle is illuminated by wavelengths of 532 and 1500 nm, and laser powers of
104 20 and 50 mW. We present measurements for aqueous aerosol particles containing the
105 atmospherically relevant inorganic solutes NaCl or $(\text{NH}_4)_2\text{SO}_4$.

106

107 **Experimental and Computational Methods**

108 Single particle cavity ring-down spectroscopy instrument

109 Figure 1 illustrates the SP-CRDS instrument, which has been described previously.^{29–33} In this
110 work, an additional NIR laser beam is included to induce droplet heating.



111

112 Figure 1: Schematic diagram of the experimental set up. AOM is an acousto-optic modulator, M1 and M2 are highly
 113 reflective mirrors constituting the ring-down cavity, PZT is a piezo ring actuator, PD is a photodiode, PBS is a
 114 polarizing beam splitter and OI an optical isolator.

115 A single aerosol particle was optically trapped in a Bessel laser beam (BB, $\lambda = 532 \text{ nm}$) while the
 116 surrounding humidity was controlled and held constant. In addition, the particle was continuously
 117 illuminated with a second laser beam ($\lambda = 473 \text{ nm}$) with a Gaussian intensity profile, from which
 118 the elastically scattered light was collected. Moreover, the particle was irradiated with a near
 119 infrared laser beam ($\lambda = 1520 \text{ nm}$) at systematically varied intensities. Finally, CRDS was used to
 120 characterize changes in the optical cross-section of the particle ($\lambda = 532 \text{ nm}$).

121 The Bessel laser beam optical trap

122 The BB was formed by passing a Gaussian 532 nm laser beam through a 2° axicon, i.e. a conically
 123 shaped lens. The resulting beam has a circularly symmetric cross-section consisting of a central
 124 core with multiple rings. The BB was focused through two lenses to reduce the BB core to 3-5 μm ,
 125 in diameter, and was reflected by a 45° mirror to propagate the beam vertically into the trapping
 126 cell. A plume of aqueous aerosol was introduced into the trapping cell from a medical nebulizer.
 127 A counter-propagating nitrogen gas flow, of controlled humidity and flow rate of $\sim 200 \text{ sccm}$,
 128 balanced the radiation pressure exerted by the BB to allow a single aerosol particle to be confined
 129 for several hours. The radii of single aerosol particles studied in this work ranged from $\sim 1 - 2 \mu\text{m}$.
 130 We ensured that a single particle was trapped in the BB by observing the elastically scattered light

131 and cavity ring-down (CRD) time. If, occasionally, more than one particle was trapped, the
132 trapping cell was evacuated and aerosol was reintroduced into the trapping cell until only a single
133 particle was trapped.

134 Retrieval of single particle real refractive index and radius

135 A Gaussian profile probe laser beam at 473 nm was aligned co-linearly with the BB through a
136 polarizing beam splitter, before being passed through a lens ($f = 50 \text{ mm}$) which weakly focused
137 the beam into the trapping cell. The probe beam diameter was $\sim 8 \times$ the diameter of the BB core.
138 The alignment of the central core of the BB and 473 nm probe beam ensured the probe beam was
139 centered on the trapped particle. A camera coupled to a $20 \times$ microscope objective situated
140 perpendicular to the direction of illumination collected the angular variation in elastically scattered
141 light, referred to the phase function (PF), from the 473 nm illumination. A 532 nm-laser line filter
142 located prior to the camera ensured that only $\lambda = 473 \text{ nm}$ light contributed to the phase function
143 images.

144 PFs were recorded every second and the experimentally measured PFs were fitted to PFs simulated
145 by Mie Theory. This procedure has been described previously.^{29,30,34,35} The elastically scattered
146 473 nm light was recorded as the NIR heating beam irradiated the droplet. The real refractive index
147 at 473 nm and the particle radius were retrieved by comparing the measured PFs with a library of
148 simulated Mie theory PFs. The parameters determining the simulated phase functions were varied
149 according to the equation:

$$n_{\lambda} = n_{\lambda,0} + \frac{n_{\lambda,1}}{a^3} + \frac{n_{\lambda,2}}{a^6} \quad 1$$

150 where n_{λ} is the refractive index at the wavelength of illumination, $n_{\lambda,0}$ is the refractive index of
151 pure water at wavelength λ , a is the particle radius, and $n_{\lambda,1}$ and $n_{\lambda,2}$ are coefficients that were
152 optimized to achieve a maximum in the mean correlation between measured and simulated PFs.
153 The optimized values of $n_{\lambda,1}$ and $n_{\lambda,2}$ were obtained by a systematic search, followed by a grid
154 search of $n_{\lambda,1}$ and $n_{\lambda,2}$ around the values associated with the highest mean Pearson correlation
155 coefficient from the initial search. Comparison of each measured PF with the simulated PF gave a
156 corresponding correlation value. The entire set of PFs has an associated mean Pearson correlation
157 coefficient, $\bar{c}(n_{\lambda})$, where $\bar{c}(n_{\lambda}) = 1$ would equate to perfect correlation between the sets of
158 measured and simulated PFs. The search parameters were refined to achieve the maximum Pearson

159 correlation, with this maximum location defining the best fit parameters of particle radii, n_λ , $n_{\lambda,1}$
160 and $n_{\lambda,2}$.

161 The RH probe was located ~ 10 cm from the droplet, which is significantly further than in
162 measurements we have previously reported. The heating beam, at 1520 nm, is focused into the
163 trapping cell where the RH probe was previously located necessitating a change in RH probe
164 location. Thus, the measurements of RH were not deemed to be reliable, as the probe was located
165 too far from the droplet trapping environment. We previously reported average n_{473} for a number
166 of aqueous inorganic species with ± 2 % uncertainty in RH.²⁹ Therefore, we instead infer the RH
167 in this study using the measured n_{473} in combination with published RI-RH parameterizations.

168 Near-IR heating of the single particle.

169 A near infrared laser beam (1520 nm, NTT Electronics, NLK1S5GAAA) was passed through an
170 optical beam shutter (Thorlabs, SH05) which opened and closed every ~ 20 seconds, thus
171 repeatedly irradiating the particle. The beam was focused by a lens ($f = 40$ mm) and then
172 propagated horizontally into the trapping cell, orthogonal to the PF and BB laser beams, and
173 towards the phase function imaging camera coupled to a high numerical aperture objective.

174 The alignment procedure for the NIR heating beam was as follows. When a droplet was trapped,
175 the elastically scattered light from the 473 nm beam was observed, using a band pass filter to
176 prevent collection of NIR light. The camera position was optimized to ensure the phase function
177 was at the center of the camera image. The band pass filter was then removed to allow coarse
178 alignment of the NIR beam with the 473 nm elastically scattered light. Finally, the filter was
179 reinstated and the NIR beam alignment was finely adjusted until the change in the positions of the
180 elastic light scattering fringes in the phase function was maximized upon exposure to the NIR
181 beam.

182 During the measurements with a single particle at constant RH, the heating beam was modulated
183 and the power controlled and varied. The trapped particle was heated for ~ 20 seconds, then the
184 heating beam was shuttered for ~ 20 seconds before the process was repeated at a different laser
185 power. The power of the heating laser was varied such that the particle experienced varying
186 magnitudes of heating, and therefore underwent varying degrees of heating-induced size change.

187 The heating laser beam waist was retrieved at the particle location from a series of measurements
188 and calculations. The beam waist of the heating beam prior to any focusing lenses was measured
189 by scrolling a razor blade mounted on a micrometer-resolution translation stage across the
190 Gaussian profile of the heating beam to determine the pre-focus beam waist and profile. The laser
191 power associated with each position of the blade was measured with a power meter. The NIR beam
192 was focused through a lens into the trapping cell and the beam waist at the focus calculated to be
193 $3.0\ \mu\text{m}$ from the lens properties and the measured pre-focus beam waist. The distance of the
194 particle from the focal point along the axis of the heating beam was retrieved as follows. A trapped
195 particle was moved along the propagation axis of the heating beam by adjusting the position of the
196 micrometer stage supporting the trapping cell. PFs were measured for the trapped particle at each
197 position along the propagation axis of the heating beam, from which the particle radius was
198 retrieved at each associated position. The change in particle radius corresponded to the position of
199 the particle in the heating beam, with a minimum in radius assumed to occur when the particle
200 experienced the focal point of the heating beam. This combination of methods allowed the heating
201 beam waist to be calculated at a given distance of the droplet from the focal point. This process
202 was repeated a number of times, giving an average beam waist at the particle's location of 81.6
203 μm , $0.5\ \text{mm}$ from focal point (for more information see the supplementary information).

204 Single particle cavity ring-down spectroscopy

205 A fourth laser beam was also centered on the aerosol droplet to provide information about any
206 change in extinction cross-section from CRDS measurements. The CRDS was conducted at a
207 wavelength of $532\ \text{nm}$ in a spectrometer which has been described previously.^{29,31,32,36} The particle
208 was centered in the CRDS beam by optimizing its vertical and horizontal positions. The particle
209 trapping height was then monitored by a camera, and a feedback loop used to control the BB laser
210 power to ensure that the particle remained in the same vertical position within the trapping cell.
211 The phase functions were recorded every second while the particle underwent the modulated
212 heating, whereas the ring down times were measured at a rate of $5\text{-}10\ \text{Hz}$.

213 CRDS was used to explore whether changes in the extinction cross-section were measurable upon
214 laser heating. We previously considered the limitations of the detectable changes in the extinction
215 cross section for a single, absorbing aerosol particle.³⁷ Here, however, the aerosol particle is non-

216 absorbing at the CRDS laser wavelength and we instead examine the consequences of absorption
217 at the wavelength of the NIR heating beam for the optical cross-section at the CRDS wavelength.

218 Modelling the size response of aqueous droplets to laser-induced heating

219 An aqueous droplet illuminated by a laser beam will be heated through absorption of radiation.
220 Constant laser irradiation raises the droplet temperature until a steady state is reached, such that
221 the energy absorbed by the droplet is equal to energy dissipated through the process of collisional
222 cooling with surrounding gas molecules. At this steady state, there is no net evaporation or
223 condensation of water at the droplet surface, and the droplet size reaches a new equilibrium value.
224 We use the droplet heating model described by Miles *et al.* to predict the size response of aqueous
225 sodium chloride droplets illuminated by an NIR laser beam of wavelength 1500 nm.²⁸ These
226 authors successfully predicted sodium chloride droplet size responses in optically tweezed aerosol
227 particles for a laser wavelength of 532 nm and used their model to retrieve the complex RI values
228 for single droplets, measuring imaginary refractive indices as small as 10^{-8} . In developing our
229 experimental set-up, we used this model to select the necessary laser wavelength and power to
230 drive observable changes in droplet size in this proof-of-concept study.

231 For an aqueous droplet of radius a illuminated by a laser of constant power P , the increase in
232 droplet temperature from an initial value T_1 to a temperature T_2 upon laser exposure is described
233 by:^{28,38,39}

$$\Delta T = T_2 - T_1 = \frac{aQ_{abs}P}{4\pi w^2 \kappa_a} \quad 2$$

234 Here, Q_{abs} is the absorption efficiency, w is the laser beam waist at the position of the droplet and
235 κ_a is the thermal conductivity of air ($0.026 \text{ W m}^{-1} \text{ K}^{-1}$ at 298 K). Mie theory is used to predict Q_{abs}
236 for an input value of particle radius, RI and wavelength. The absorption efficiency contains
237 structure from interference and so-called ripple contributions; for illumination wavelengths
238 smaller than the droplet size, sharp resonances in Q_{abs} can cause large increases in the droplet
239 temperature.^{28,40,41}

240 At equilibrium, the vapor pressure of water above a solution droplet surface equals the partial
241 pressure of water in the gas phase. Once heated, the solution droplet will evaporate to regain this
242 thermodynamic criterion for equilibrium: the increase in vapor pressure from heating is
243 counteracted by a vapor pressure reduction due to the increasing concentration of solutes within

244 the droplet with decreasing size. The Clausius-Clapeyron equation relates the change in vapor
 245 pressure of the solution to a change in temperature:

$$\ln \left[\frac{p(T_2)}{p(T_1)} \right] = \frac{\Delta H_{vap}}{R} \frac{T_2 - T_1}{T_1 T_2} \quad 3$$

246 in which ΔH_{vap} is the enthalpy of vaporisation of the aqueous solution and R is the molar gas
 247 constant. Assuming changes in the droplet temperature from laser-induced heating are small,
 248 Equation 3 simplifies to:

$$\ln \left[\frac{p(T_2)}{p(T_1)} \right] = \frac{\Delta H_{vap}}{R} \frac{\Delta T}{T_1^2} \quad 4$$

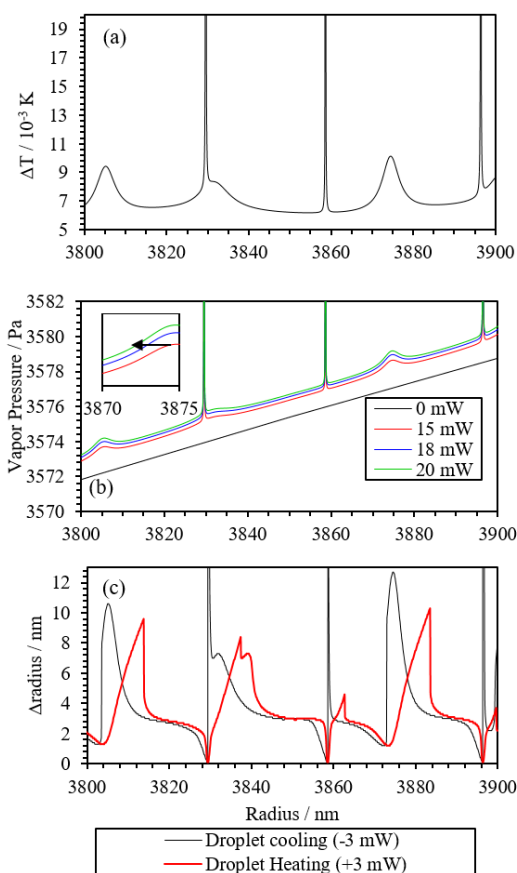
249 with ΔT described by Equation 2. The absolute vapor pressure depends on the activity of water in
 250 the solution droplet, a_w , which decreases as water evaporates and the droplet decreases in volume.
 251 We incorporate the dependence of vapor pressure on a_w , and define $T_1 = T_a$, the ambient
 252 temperature T_a in the absence of laser heating, to obtain the vapor pressure of the heated droplet:

$$p(T_2) = a_w p_{sat}(T_a) \exp \left[\frac{\Delta H_{vap}}{R} \frac{\Delta T}{T_a^2} \right] \quad 5$$

253 Here, $p_{sat}(T_a)$ is the saturation vapour pressure of water above a flat surface at ambient
 254 temperature (3235 Pa at 298 K). We used the E-AIM model to describe the dependence of droplet
 255 size and solute concentration on a_w .^{42,43} We then used calculations from E-AIM to relate the radial
 256 growth factor (the ratio of the radius for the solution droplet to that corresponding to the dry salt)
 257 to a_w . This allowed simulations of $p(T_2)$ at all values of a_w (and hence radii) over which the solution
 258 droplet exists, i.e. from the efflorescence water activity (~ 0.45 for sodium chloride) to 1.00.

259 Here, we first verify our model by comparing predictions for $\lambda = 532$ nm with previous data
 260 reported by Miles *et al.*, before considering the influence of NIR illumination ($\lambda = 1500$ nm) on
 261 particle heating. The model calculations were validated against the simulations of Miles *et al.* using
 262 the parameters for their $\lambda = 532$ nm optical tweezer experiments.²⁸ The initial droplet size was set
 263 as 3913.3 nm at a corresponding water activity of $a_w = 0.9775$ to represent typical droplet
 264 conditions in the experiments. ΔH_{vap} was set to 44×10^3 J mol⁻¹ (i.e. close to the 44.24 kJ mol⁻¹
 265 value for a saturated salt solution), T_a was fixed at 300 K and $w = 4$ μ m. The simulations by Miles
 266 *et al.* use Mie-Debye spherical aberration theory to predict Q_{abs} for a focused Gaussian beam, while

267 we used Mie theory to simulation Q_{abs} . We described the real RI of the sodium chloride solution
 268 droplet and its dependence on a_w using the parameterization we reported recently,²⁹ although Miles
 269 *et al.* used a parameterization based on electrodynamic balance measurements,⁴⁴ and set the
 270 imaginary RI to 2.5×10^{-9} . Figure 2(a) shows our calculations of ΔT for $\lambda = 532$ nm and a laser
 271 power of 20 mW, which gives a temperature elevation of 10s of millikelvin, depending on starting
 272 droplet size. Based on these temperature perturbations, Figure 2(b) shows the calculated change in
 273 droplet vapor pressure for laser powers of 0, 15, 18 and 20 mW with change in droplet size. The
 274 introduction of the laser heating beam induces significant changes to the vapor pressure with
 275 resonant enhancement by whispering gallery modes at particular droplet sizes. Our calculations of
 276 vapor pressure agree well with those reported by Miles *et al.*



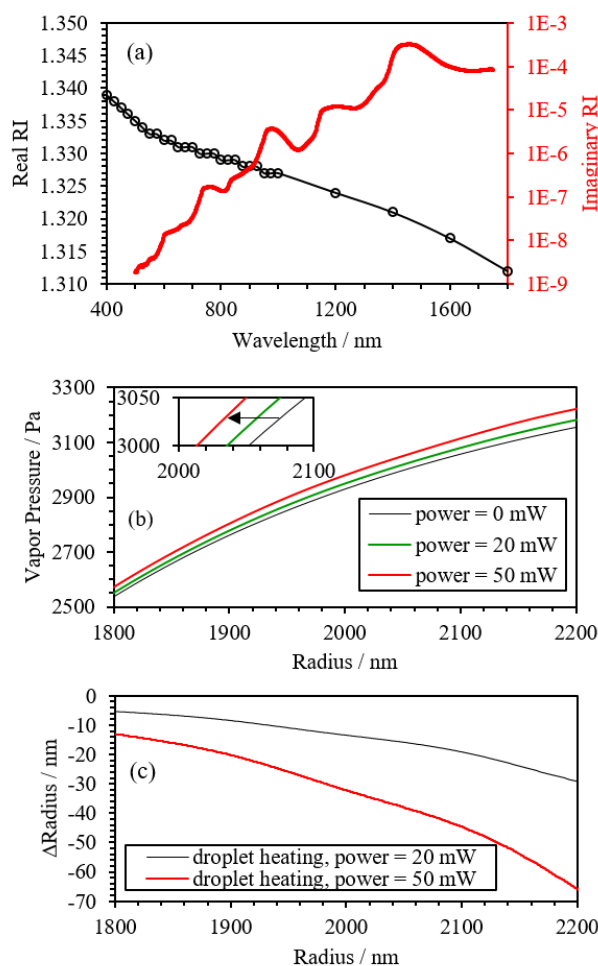
277
 278 Figure 2: Simulated droplet heating behavior for an aqueous NaCl droplet at an initial $a_w = 0.9775$, irradiation
 279 wavelength $\lambda = 532$ nm, and beam waist $w = 4$ μm . (a) the variation in ΔT with droplet radius for $P = 20$ mW; (b)
 280 calculations of the vapor pressure variation with droplet radius for values of P of 0, 15, 18 and 20 mW; (c) the predicted
 281 change in droplet radius (Δradius) for the cases of a decrease in laser power from 18 mW to 15 mW (black line) and
 282 an increase in laser power from 15 mW to 18 mW (red line).

283 We also calculated the change in radius (Δ radius) expected when the laser power is modulated
284 between 15 mW and 18 mW. The Δ radius values are calculated from an isobaric line on the vapor
285 pressure – radius plot (Figure 2(b)) linking two curves corresponding to different laser powers.
286 The droplet radius axis in Figure 2(c) corresponds to the initial radii of a number of simulated
287 droplets before stepping the laser power and the induced heating. Once equilibrated in size, the
288 droplet has the same vapor pressure before and after the step in laser power, but this vapor pressure
289 is a combination of different degrees of elevation (by heating) and reduction (from solute effects
290 associated with droplet size changes). Figure 2(c) also shows the Δ radius for the opposite case of
291 increasing the laser power (heating) by 3 mW, demonstrating the non-reversible changes in
292 Δ radius caused by the resonance structure. There are multiple radii at which equal vapor pressure
293 is attained, and the radius change achieved will differ depending on whether the particle is cooling,
294 and the radius is increasing from condensational growth, or the particle is being heated, and the
295 radius is decreasing from evaporative loss.

296 Having verified that our laser-induced droplet heating model correctly predicts changes in droplet
297 size, we then used it to investigate whether we could resolve changes in droplet size induced by λ
298 = 532 nm laser heating from the Bessel beam optical trap in our SP-CRDS instrument. The change
299 in power density that we can induce in our BB optical trap is comparable to those achievable in
300 the optical tweezer experiments of Miles *et al.* However, we are limited to a maximum RH of ~
301 80% in our instrument, caused by the dilution of ambient air by the dry N₂ gas purge flows that
302 pass over the CRDS mirrors. Compared to the RH values of 97.75% used in the experiments of
303 Miles *et al.*, our SP-CRDS measurements occur within a regime where the radial growth factor
304 has a very low sensitivity to a_w . Using $w = 2 \mu\text{m}$, a change in laser power from 30 mW to 35 mW
305 (a typical range achievable for the Bessel beam core power), an initial NaCl particle radius of 2000
306 nm (the largest typical size we trap in our SP-CRDS instrument) for an initial a_w of 0.8, our heating
307 model predicts Δ radius of < 2 nm. This change is too small to resolve with the precision of size
308 retrievals from PFs. Therefore, we now investigate the effectiveness of laser-induced heating using
309 a NIR laser emitting at a wavelength matching a strong absorption band for water in inducing size
310 changes sufficient for detection with PF measurements.

311
312 The NIR laser heating experiments reported here drive water evaporation from an aqueous sodium
313 chloride or ammonium sulfate droplet confined in the BB trap of an SP-CRDS instrument. The

314 heating laser has a much broader focus than in the optical tweezers measurements of Miles *et al.*,
 315 and the droplet is smaller in size. Instead of investigating the optical absorption in the visible, we
 316 measure the imaginary component of the refractive index at 1500 nm. Figure 3(a) shows the
 317 variation in the complex RI components with wavelength for water.^{45,46} The imaginary RI
 318 increases by ~ 3 orders of magnitude from a wavelength of 532 to 1064 nm, and increases by a
 319 further 2 orders of magnitude from 1064 to 1500 nm, with a value of $k = 2.57 \times 10^{-4}$ at $\lambda = 1500$
 320 nm. The simulations reported below correspond to a NIR heating beam with $\lambda = 1500$ nm.



321
 322 Figure 3: (a) The variation in the real RI⁴⁵ and imaginary RI⁴⁶ for water over the wavelength range 400 – 1800 nm.
 323 Lines are to guide the eye. (b) The calculated vapor pressure for an aqueous NaCl droplet with an initial radius of
 324 1800 nm at an initial a_w of 0.8 upon illumination with a $\lambda = 1500$ nm, $w = 100$ μ m laser beam using P values of 0, 20
 325 and 50 mW. (c) The calculated Δ radius using the simulations in (b), for a droplet heated from an initial state
 326 corresponding to $P = 0$ mW.

327 We performed simulations of the droplet vapor pressure and Δ radius for $\lambda = 1500$ nm and $w = 100$
 328 μ m. For these simulations, we used the aforementioned heating model parameters and methods.

329 To describe the complex RI of aqueous NaCl droplets at IR wavelengths, we used the RI
330 descriptions for pure water as reported in Figure 3(a). The real RI was set to 1.319 and the
331 imaginary RI set to 2.57×10^{-4} . The reference droplet radius was selected to be 1800 nm at an initial
332 a_w of 0.8 equal to an environmental RH of 80 %, representing typical values for a droplet confined
333 in the SP-CRDS instrument at high RH. We repeated the simulations for the three laser powers of
334 0, 20 and 50 mW. Figure 3(b) shows the predicted vapor pressure curves over the droplet radius
335 range 1800 – 2200 nm. Unlike the shorter wavelength simulations, there is an absence of resonant
336 structure in the vapor pressures curves because of the long wavelength of the NIR beam compared
337 to the droplet radius, and the much larger value of the imaginary RI, which damps resonant
338 coupling into whispering gallery modes. We calculated Δ radius in the heating direction, from a
339 starting droplet with no heating to a droplet illuminated at powers of either 20 or 50 mW. Figure
340 3(c) shows the expected change in droplet radius upon exposure to the heating beam, with
341 representative values of Δ radius of 13.5 nm and 32 nm for $P = 20$ mW and $P = 50$ mW,
342 respectively. These size changes are sufficient for detection by PF imaging.

343

344

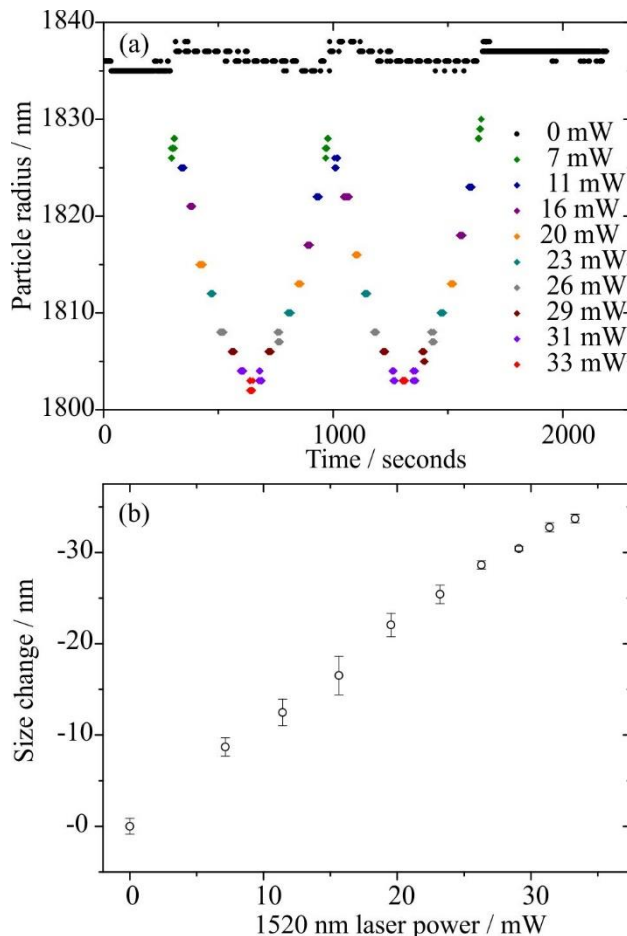
345 **Results and discussion**

346 Near-IR heating of single aerosol particles at high relative humidity

347 Single aerosol particles composed of both aqueous ammonium sulfate and sodium chloride have
348 been studied. Each particle was trapped, and held at (near) constant RH to retrieve k as a function
349 of RH. The heating laser beam irradiated the particle while the power was modulated and
350 systematically varied in power. Laser illumination of the droplet caused the droplet temperature to
351 increase, thus driving evaporation of water, and an associated heating-induced size change was
352 measured. At each laser power, the 1520 nm laser irradiated the droplet for ~ 20 seconds, which
353 was sufficient time to allow the particle to achieve a steady size, with no further net condensation
354 or evaporation. Figure 4(a) shows the radius response of a single aqueous sodium chloride particle
355 to heating. Upon initiation of heating, the droplet evaporated to its new equilibrium size within 1
356 second, the limiting detection timescale of PF measurements. A strong correlation can be seen
357 between the incident laser power and the volume of water lost from the droplet, in Figure 4(a) and

358 (b). The radius of the particle reverted to the original size once the heating beam was attenuated to
359 zero power (black points).

360



361

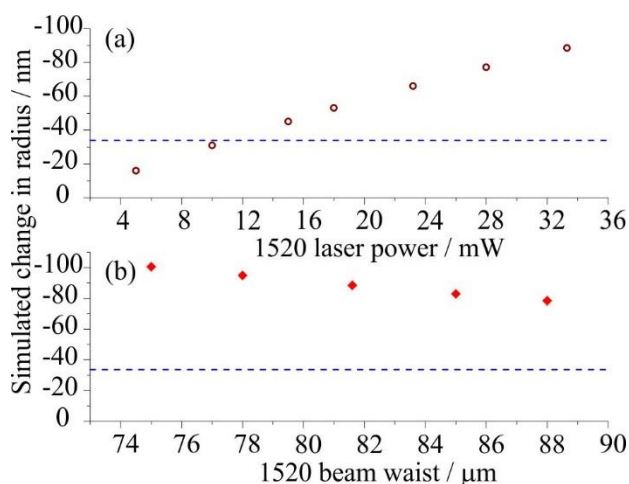
362 Figure 4: Irradiation of an aqueous NaCl droplet with a 1520-nm laser beam. (a) Changes to the radius of the single
363 aerosol particle as the laser power is varied (indicated by the colored data points). (b) The average change in particle
364 radius as a function of heating laser power. The error bars indicate the standard deviation in the derived radius.

365

366 Comparing the simulated NIR heating-induced size change to the measured size change

367 The heating-induced size changes measured from PFs were compared to the modelled size
368 changes. The simulations required inputs of beam waist (81.6 μm , estimated with the method
369 outlined earlier and described more extensively in the Supplementary Information) and initial
370 water activity ($a_w = 0.89$, for the particles in Figure 4). The particle radius was 1836 nm without

371 1520 nm irradiation and the maximum laser power used was 33 mW. However, the calculated size
 372 change was approximately double the experimentally measured size change at 33 mW and this
 373 was found to be the case for all particles studied. This discrepancy (of ~ 41 nm, for the particle
 374 presented in Figure 5) is significantly larger than the uncertainty of ± 0.5 nm associated with PF
 375 analysis, suggesting that one of the parameters required for the heating simulation was not correct.
 376 The $\pm 2\%$ uncertainty associated with the retrieved RH only accounts for ± 0.5 nm of size change.
 377 The modelled heating-induced size change was more sensitive to the values of beam waist or laser
 378 power. Figure 5 shows the sensitivity in the simulated change in radius to these model inputs for
 379 the single highest power measurement. In Figure 5(a), the simulated value of the laser power was
 380 varied from 5 – 33 mW with the beam waist set at $81.6 \mu\text{m}$. In Figure 5(b), the simulated 1520 nm
 381 beam waist was varied from $75 - 88 \mu\text{m}$ while the laser power was held constant at 33 mW. The
 382 resultant changes in radius predicted by the model are compared to the measured change in radius
 383 of 33 nm recorded at the highest level of NIR power, $P = 33$ mW (indicated by the blue dashed
 384 line).



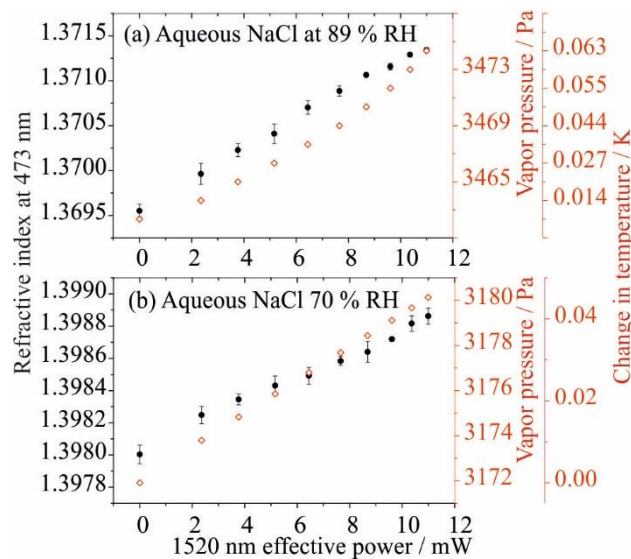
385
 386 Figure 5: The variation in the modelled heating-induced size change (with inputs of initial size = 1836 nm, $a_w = 0.89$,
 387 initial laser power = 0 mW) as the following input parameters were varied: (a) final laser power (mW), with the beam
 388 waist set to $81.6 \mu\text{m}$ and (b) beam waist ($75 - 88 \mu\text{m}$), with the final laser power set at 33 mW. The experimentally
 389 measured size change of a droplet of 1836 nm at $a_w = 0.89$ and laser power 33 mW is indicated by the dashed blue line.

390 From Figure 5, the simulated heating-induced size change is significantly more sensitive to
 391 changes in the input laser power than the input heating beam waist. The range of values of beam
 392 waist chosen corresponds to the uncertainty associated with the measurements of the NIR beam
 393 waist. Therefore, we deduce that the particle must be sampling less than the expected fraction of
 394 the full laser power (33 mW) calculated by comparing the beam waist and the particle radius.

395 Instead, we must base our analysis on inferring changes in absorption and k with RH and size
396 relative to measurements for a droplet at one reference RH, chosen here to be the highest RH. At
397 this reference RH, we assume that the value of k is equal to that of pure water at the highest RH
398 and calculates the effective laser power that gives the observed size change at this RH. This
399 retrieved value of effective laser power is then input for measurements at lower RHs while k_{1520} is
400 varied in the model simulations.

401 For the data presented in Figure 4, the derived effective total laser power incident on the trapped
402 aqueous NaCl droplet corresponds to 11.0 mW, which is a third of the value expected based on
403 the measured total power output from the 1520 nm beam. This scaling of the actual to effective
404 laser power was retained in further model simulations for all subsequent particle measurements at
405 lower humidities. The scaling accounts for the imperfect transverse and axial positioning of the
406 droplet in the focused Gaussian beam; although a more exact model could be implemented, the
407 current challenge is one of experimental alignment. A particle of $\sim 1 \mu\text{m}$ size held within a
408 vertically propagating Bessel beam core of similar size and co-propagating beam for PF
409 determination, must be aligned simultaneous with a horizontally propagating CRD beam of waist
410 $\sim 200 \mu\text{m}$, the orthogonally propagating NIR laser beam with a focal waist estimated an $< 10 \mu\text{m}$.
411 For particles at lower humidities (i.e. all particles other than the initial reference particle from
412 which the effective laser power was calculated), the value of k_{1520} input into the model was varied,
413 thus allowing a relative change in k_{1520} from that of pure water to be calculated. This approach
414 does enable the relationships between k_{1520} , droplet size and RH to be examined.

415 Figure 6 shows the outcome of experimentally varying the laser power on the value of n_{473}
416 retrieved from the PF measurements at 473 nm, and the modelled temperature and vapor pressure
417 for two aqueous NaCl droplets held at 89 % and 70% RH. As the NIR laser power illuminating
418 the particle increases, n_{473} also increases, as expected for a decreasing droplet size and increasing
419 solute concentration. Similarly, the retrieved n_{473} of the particle at 70% RH is higher than that of
420 the particle at 89% RH, again due to the higher concentration of solute at lower RH. The
421 concomitant changes in vapor pressure and temperature for each particle were retrieved from
422 model simulations (at the appropriate conditions of e.g. RH). The simulated change in particle
423 temperature is always $< 0.1 \text{ K}$, but is larger for higher NIR laser powers, as expected.



424

425 Figure 6: The effect of 1520 nm laser power (scaled to an effective power, as described in the main text) on the average
 426 (from up to 7 measurements at each laser power) real refractive index retrieved from fitting PFs at $\lambda = 473$ nm to Mie
 427 theory predictions (black data points), and the simulated vapor pressure (red data points) and corresponding
 428 temperature change (additional axis) for 2 different aqueous NaCl particles held at different humidities.

429 We report average values of n_{473} in Figure 6, retrieved from multiple measurements of n_{473} at each
 430 effective laser power as the power was systematically increased and decreased and repeatedly
 431 modulated; a standard deviation of $< \pm 0.00006$ is indicated by the error bars. At any one laser
 432 power, there is variation in n_{473} because the particle was exposed to each laser power multiple
 433 times (shown in Figure 4) over ~ 2000 seconds. Over the course of the measurement, drift in RH
 434 alters the particle composition and thus the retrieved n_{473} . Considering the timescale of the
 435 experiment and slight variations in RH, the modest standard deviations in retrieved n_{473} values
 436 illustrate the precision of our technique. The changes in temperature and vapor pressure (red data
 437 points in Figure 6) are inferred from the model simulations.

438

439 Retrieving the imaginary component of the refractive index of aqueous NaCl and $(\text{NH}_4)_2\text{SO}_4$
 440 aerosol particles with varying humidity

441 Single particles composed of aqueous NaCl were held at a discrete RH while the laser power
 442 irradiating the particle was varied. The heating-induced size-change was normalized by converting
 443 it to a change in growth factor which allowed the variation in size change as a function of RH to

444 be examined over many droplets of different absolute size. The radial growth factor is defined as
 445 the ratio of the wet droplet radius to the dry particle radius and the change is growth factor (ΔGF)
 446 is given by:

$$\Delta GF = \frac{a_0 - a_x}{a_{dry}} \quad 6$$

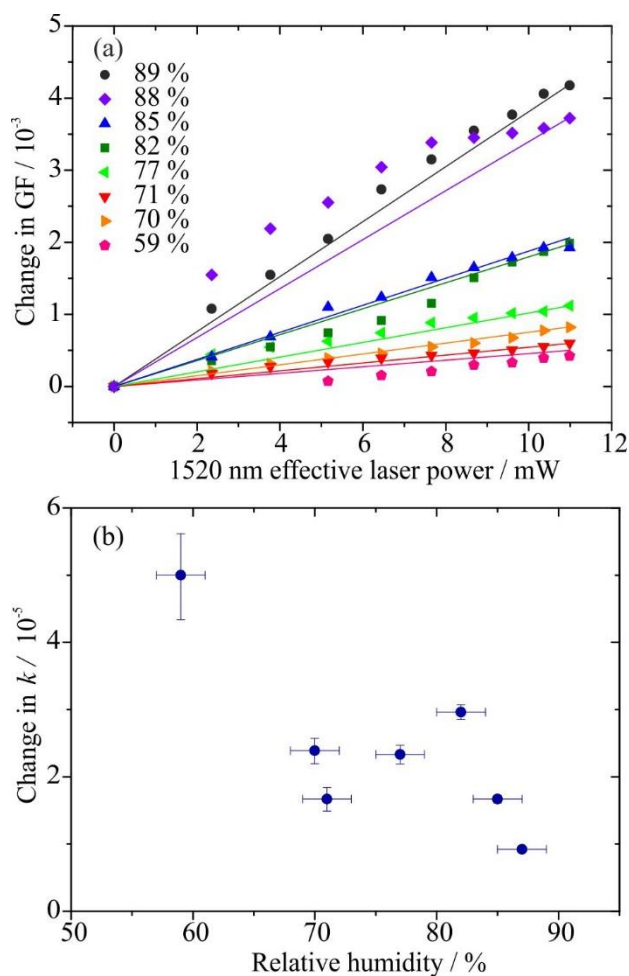
447 where a_0 is the radius of a given particle when not illuminated by the NIR beam, a_x is the radius
 448 of the same particle at a given NIR laser power of $P = x$ mW, and a_{dry} is the dry size calculated for
 449 each particle. The variation in the radial growth factor with RH was calculated from the E-AIM
 450 model.^{42,43} Then, from comparing the calculated growth factor dependence on RH with the
 451 experimental variation in wet droplet size with RH in the absence of the NIR beam, the dry particle
 452 size was determined. Finally, the change in growth factor on illumination was calculated from
 453 Equation (6).

454 Figure 7(a) shows the change in GF for 7 different droplets held at RHs in the range 59 – 89 %
 455 while the power of the NIR beam was varied. The magnitude of change in GF can be seen to
 456 depend systematically on RH. The RH is indicative of the composition of the particle: at lower
 457 RHs, the particle solute concentration is higher (a_w is lower), and greater laser power is required
 458 to drive the same amount of water evaporation, compared to an equivalent sized particle at higher
 459 RH. Therefore, the relative magnitude of change in GF is smaller as the surrounding RH decreases.

460 The variation in the imaginary component of the refractive index with RH was retrieved by
 461 simulating size changes for a range of Δk_{1520} values, and comparing the changes in simulated and
 462 measured size changes with laser power at each RH. The retrieved value of k_{1520} represents the
 463 change in k_{1520} (Δk_{1520}) from that at the reference RH rather than an absolute value, shown in
 464 Equation 7:

$$\Delta k_{1520} = k_{1520}(\text{measurement at RH}) - k_{1520}(\text{reference}) \quad 7$$

465 where $k_{1520}(\text{reference})$ is the imaginary component of pure water that is input in the reference
 466 measurement at the highest humidity, from which the effective laser power is determined. In this
 467 analysis, the other input parameters were kept constant while Δk_{1520} was varied. The results are
 468 shown in Figure 7(b). Although this method does not give the absolute value of k_{1520} it does enable
 469 the dependence of Δk_{1520} on RH to be examined.



470

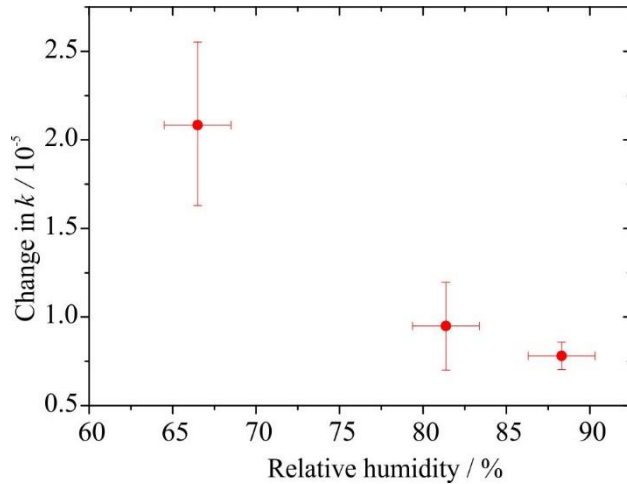
471 Figure 7: (a) Variation in the change of growth factor for aqueous NaCl particles as a function of the effective heating
 472 laser beam power for RHs from 59-89%. The lines correspond to the model prediction of the particle heating-induced
 473 size change converted to the GF domain; (b) the retrieved change in k_{1520} for aqueous NaCl particles as a function of
 474 RH. The x-axis error bars correspond to the $\pm 2\%$ uncertainty in RH, and the y-axis error bars represent the uncertainty
 475 associated with the retrieved size from PF fitting.

476 The data plotted in Figure 7(b) suggest a change in k_{1520} for aqueous NaCl droplets as the humidity
 477 decreases. This trend is indicative of the particle composition, which is in equilibrium with the
 478 surrounding gas phase: as the humidity decreases, the water content of the particle also decreases,
 479 which increases the solute concentration. We assume that the light absorption responsible for the
 480 observed Δk_{1520} is caused by impurities in the NaCl solute, because NaCl does not absorb at 1520
 481 nm, and this absorption is additional to that of pure water (which is already accounted for in the
 482 initial simulations of the reference particle).⁴⁷ Miles *et al.* also studied the light absorption of single
 483 aqueous NaCl particles at 532 nm with Raman spectroscopy.²⁸ Their retrieved values of k_{532} were

484 larger than that of pure water, and this difference was also attributed to the presence of absorbing
485 impurities.²⁸

486 The error bars in Figure 7(b) represent the uncertainty associated with the inferred RH and the
487 retrieved particle size. Fitting the measured PFs with Mie theory yielded the radius and n_{473} values
488 for each particle. Measurements were only included in this work when $\bar{c}(n_{473}) > 0.99$. The
489 uncertainty in the size of the particle retrieved from PF measurements was ± 0.5 nm. The impact
490 of this uncertainty in the retrieved value of Δk_{1520} was assessed by fitting Δk_{1520} to the
491 experimentally measured size change ± 0.5 nm. The resulting uncertainties in the retrieved values
492 of Δk_{1520} are shown in Figure 7(b). The smaller the initial size of the droplet, the larger is the
493 uncertainty in Δk_{1520} .

494 Figure 8 shows the variation in the Δk_{1520} for a single aqueous $(\text{NH}_4)_2\text{SO}_4$ particle over a range of
495 RHs, with the highest RH measurement again serving to provide the reference point for the scaling
496 needed to deduce the effective NIR laser beam power. Unlike the case of aqueous sodium chloride
497 aerosol shown in Figure 7, these measurements were made on the same particle and clearly show
498 that Δk_{1520} increases as RH decreases. The magnitude of the change in k_{1520} with RH is comparable
499 to that of aqueous NaCl. The variation of k_λ with wavelength for $(\text{NH}_4)_2\text{SO}_4$ crystals was reported
500 previously, and the nearest value to our measurement wavelength is at $\lambda = 1500$ nm where $k_{1500} =$
501 3.4×10^{-5} .⁴⁸ This is of the same order of magnitude as our reported change in k_{1520} from that of
502 water with decreasing RH. Measurements of the absolute imaginary component of the refractive
503 index are of greater interest than a relative measure of Δk_{1520} . However, here the importance of
504 measuring the variation in Δk_{1520} with RH, even for very weakly absorbing species, is highlighted.
505 Further work will endeavor to measure k_λ directly as a function of RH, for a wider range of droplet
506 compositions, to parameterize the dependence of k_λ on RH.



507

508 Figure 8: The change in the relative value of k_{1520} for a single aqueous $(\text{NH}_4)_2\text{SO}_4$ particle held at a range of humidities.

509 Measurements of the extinction cross-section of a heated single particle

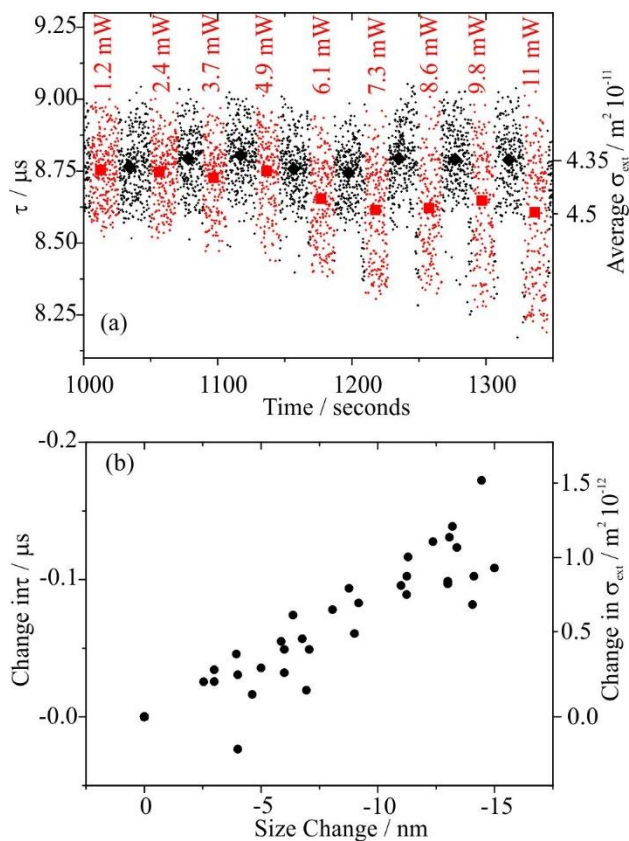
510 Single particle cavity ring-down spectroscopy measurements were performed for each particle as
 511 it was irradiated with the heating beam, and a section of a measurement is shown in Figure 9(a) as
 512 an example. The cavity ring-down times, τ , are used to determine the extinction cross-section of
 513 the single particle, where:

$$\sigma_{ext} = \frac{L\pi w^2}{c} \left(\frac{1}{\tau} - \frac{1}{\tau_0} \right) \quad 8$$

514 where L is the length of the optical cavity, w is the beam waist (of the CRD beam, and estimated
 515 as 0.24 mm in later estimates of σ_{ext}), and τ_0 the cavity ring down time of the optical cavity in the
 516 absence of the droplet.⁴⁹ CRDS measurements were made at a wavelength of 532 nm, where the
 517 particle is non-absorbing. Figure 9(a) shows variation in τ as the particle was heated by the NIR
 518 laser beam, and illustrates the sensitivity to changes in the particle extinction cross-section induced
 519 by the heating. The changes in the recorded cavity ring-down times increase as the power of the
 520 heating beam increases. The fluctuations in τ are a consequence of Brownian motion of the aerosol
 521 particle within the BB trap.^{32,50}

522

523



524

525 Figure 9: (a) The cavity ring-down times, τ , of a single aqueous NaCl particle as it was heated by a 1520 nm beam
 526 (red points) decrease compared to when the 1520 nm beam was blocked (black points). The 1520 nm effective laser
 527 power is indicated with red labels. The average τ values at each effective laser power are shown by large red squares,
 528 and when the NIR beam is off by the large black diamonds. The average (large red and black) points also correspond
 529 to the average estimated σ_{ext} indicated on the corresponding y-axis. (b) The measured τ values and the associated
 530 estimated change in σ_{ext} are shown as a function of the particle size change, retrieved from PF measurements, as a
 531 result of modulated heating.

532 Figure 9(a) shows the average measured ring-down time τ , which decreases as the particle is
 533 irradiated with increasing NIR illumination. As the particle size decreases, its smaller geometric
 534 cross section might be expected to cause an increase in the τ value. However, the τ value is
 535 determined by the extinction cross section, not the geometric cross section. These two parameters
 536 are connected by the extinction efficiency, Q_{ext} , in which is defined in Equation 9. Q_{ext} is a function
 537 of the size parameter, χ (shown in Equation 10).

$$Q_{ext} = \frac{\sigma_{ext}}{\sigma_{geom}} \quad 9$$

$$\chi = \frac{\pi D}{\lambda}$$

538 Here, D is the particle diameter and λ is the wavelength of illumination. The extinction efficiency
539 varies with size parameter; thus, as the particle is heated and the size parameter changes, the
540 particle will exhibit different extinction efficiencies. In the size parameter range of the particle
541 considered in the current example, as the particle is heated the extinction efficiency increases with
542 decrease in size. The resulting increase in σ_{ext} causes the observed changes to τ values upon heating.

543 The rapid heating-induced size response was generally recorded more rapidly by CRDS than by
544 the PF measurements, and observed before the change in the electronic signal reporting the status
545 of the shutter controlling the heating beam was registered. Both the PF and shutter status data were
546 collected every second. This effect is particularly evident in Figure 9(a) at times around 1210
547 seconds, where the τ values have changed, but the data points are still color-coded as black. Thus,
548 the CRDS data illustrate the rapid size response of the droplets to irradiation by the heating beam,
549 and indicate the benefits that would derive from measuring PFs and the shutter status at intervals
550 of < 1 second.

551 Figure 9(b) shows the consequences of changes in the power of the heating beam for measured τ
552 values, and change in σ_{ext} values from CRDS and droplet sizes measured from PFs. There is a clear
553 correlation between the changes in τ , σ_{ext} and particle size change induced by droplet heating, each
554 of which is retrieved from separate measurement techniques (CRDS and PFs respectively). This
555 trend reinforces the sensitivity of both phase function measurements and cavity ring-down
556 spectroscopy to changes in the size of single aerosol particles, and further illustrates the
557 complementary use of these techniques. Here we have demonstrated the possibility of providing
558 concurrent extinction cross-section measurements by CRDS when exploring optically induced
559 heating. A fuller analysis of this approach will be the focus of a subsequent paper.

560

561 Conclusions:

562 Droplet heating by a NIR laser has been combined with our previously reported single-particle
563 trapping and observation methods to measure RH-dependent changes in complex refractive index
564 of weakly absorbing single aerosol particles. The absorption of 1520-nm laser radiation by single
565 particles composed of aqueous NaCl or $(\text{NH}_4)_2\text{SO}_4$ has been reported at a range of discrete RHs.

566 The size and real component of the refractive index of the particle were retrieved from phase
567 function measurements, and the absorption of a particle relative to a water droplet was calculated
568 from the change in particle size upon heating. The positioning of the single particle in the heating
569 beam proved to be crucial in quantitatively accounting for the size change upon heating and this
570 challenge must be addressed in future work, despite the critical tolerances in aligning multiple
571 laser beams with a trapped droplet that must be achieved. However, here we have developed a
572 method to scale the incident laser power to quantify the actual power irradiating the particle and
573 to retrieve relative changes in absorption. Multiple measurements of single particles of aqueous
574 NaCl, and a single aqueous $(\text{NH}_4)_2\text{SO}_4$ particle showed an increase in k_{1520} relative to that of water
575 with decreasing RH. This greater absorption at 1520 nm at lower RHs was attributed to impurities
576 in the solute. The measurements illustrate the capability of the system to retrieve Δk_{1520} values for
577 very weakly absorbing aerosol. Despite determining a relative change in k_{1520} rather than an
578 absolute value, the data highlight the variation in the absorption of aerosol particles with RH, thus
579 emphasizing this dependence as an additional factor to be considered when including aerosol
580 optical properties in radiative transfer models.

581 The detection of changes to the extinction cross-section of a single particle of radius 1-2 μm as the
582 heating beam was modulated demonstrates the sensitivity of our SP-CRDS technique. The changes
583 in geometric cross-section derived from phase function measurements, and changes in extinction
584 cross-section from cavity ring-down spectroscopy, illustrate the complementary nature of these
585 analysis methods. In addition, the CRDS measurements can be made with extremely high time
586 resolution. Such measurements could be invaluable in measuring kinetic parameters for water
587 condensation/evaporation, for example in retrieving the value of the mass accommodation
588 coefficient from measurements on single particles that are much smaller than previously
589 studied.^{51,52} In addition, these measurements will allow us to look at the mechanism inherent to
590 photoacoustic spectroscopy, potentially allowing us to study the ambiguities that arise in PAS
591 measurements at elevated RH when the photoacoustic signal is a product of mass transfer from an
592 evaporating droplet as well as heat transport.⁵³ Further applications will include retrieval of
593 complex refractive index information for more strongly absorbing aerosol species for inclusion in
594 radiative transfer models.

595

596 Supporting Information

597 The Supporting Information provides further description of the heating laser beam waist retrieval,
598 and further discussion on the retrieval of the effective laser power.

599 Acknowledgments

600 REW acknowledges funding from GW4+ DTP from NERC (NE/L002434/1) and support from the
601 Aerosol Society in the form of the CN Davies Award. MIC acknowledges funding from NERC
602 and the RSC through an Analytical Trust Fund studentship (NE/J01754X/1) and support from the
603 Aerosol Society in the form of a CN Davies award.

604 References

- 605 (1) Boucher, O.; Randall, D.; Artaxo, P.; Bretherton, C.; Feingold, G.; Forster, P.; Kerminen,
606 V.-M. V.-M.; Kondo, Y.; Liao, H.; Lohmann, U.; et al. Clouds and Aerosols. *Clim.*
607 *Chang. 2013 Phys. Sci. Basis. Contrib. Work. Gr. I to Fifth Assess. Rep. Intergov. Panel*
608 *Clim. Chang.* **2013**, 571–657.
- 609 (2) Zarzana, K. J.; Cappa, C. D.; Tolbert, M. A. Sensitivity of Aerosol Refractive Index
610 Retrievals Using Optical Spectroscopy. *Aerosol Sci. Technol.* **2014**, 48 (11), 1133–1144.
- 611 (3) Moise, T.; Flores, J. M.; Rudich, Y. Optical Properties of Secondary Organic Aerosols and
612 Their Changes by Chemical Processes. *Chem. Rev.* **2015**, 115 (10), 4400–4439.
- 613 (4) Wang, L.; Wang, W. G.; Ge, M. F. Extinction Efficiencies of Mixed Aerosols Measured
614 by Aerosol Cavity Ring down Spectrometry. *Chinese Sci. Bull.* **2012**, 57 (20), 2567–2573.
- 615 (5) Beaver, M.; Garland, R. A Laboratory Investigation of the Relative Humidity Dependence
616 of Light Extinction by Organic Compounds from Lignin Combustion. *Environ. Res. Lett.*
617 **2008**, 3 (4), 045003.1-045003.8.
- 618 (6) Veghte, D. P.; Altaf, M. B.; Haines, J. D.; Freedman, M. A. Optical Properties of Non-
619 Absorbing Mineral Dust Components and Mixtures. *Aerosol Sci. Technol.* **2016**, 6826, 1–
620 14.
- 621 (7) Baynard, T.; Garland, R. M.; Ravishankara, A. R.; Tolbert, M. A.; Lovejoy, E. R. Key
622 Factors Influencing the Relative Humidity Dependence of Aerosol Light Scattering.

- 623 *Geophys. Res. Lett.* **2006**, *33* (6), 3–6.
- 624 (8) Li, K.; Wang, W.; Ge, M.; Li, J.; Wang, D. Optical Properties of Secondary Organic
625 Aerosols Generated by Photooxidation of Aromatic Hydrocarbons. *Sci Rep* **2014**, *4*,
626 4922.1-4922.9.
- 627 (9) Mason, B. J.; King, S.-J.; Miles, R. E. H.; Manfred, K. M.; Rickards, A. M. J.; Kim, J.;
628 Reid, J. P.; Orr-Ewing, A. J. Comparison of the Accuracy of Aerosol Refractive Index
629 Measurements from Single Particle and Ensemble Techniques. *J. Phys. Chem. A* **2012**,
630 *116* (33), 8547–8556.
- 631 (10) Riziq, A. A.; Erlick, C.; Dinar, E.; Rudich, Y. Optical Properties of Absorbing and Non-
632 Absorbing Aerosols Retrieved by Cavity Ring down (CRD) Spectroscopy. *Atmos. Chem.*
633 *Phys. Discuss.* **2006**, *6* (6), 12347–12387.
- 634 (11) Dinar, E.; Abo Riziq, A.; Spindler, C.; Erlick, C.; Kiss, G.; Rudich, Y. The Complex
635 Refractive Index of Atmospheric and Model Humic-Like Substances (HULIS) Retrieved
636 by a Cavity Ring Down Aerosol Spectrometer (CRD-AS). *Faraday Discuss.* **2008**, *137*,
637 279–295.
- 638 (12) Michel Flores, J.; Bar-Or, R. Z.; Bluvshstein, N.; Abo-Riziq, A.; Kostinski, A.; Borrmann,
639 S.; Koren, I.; Koren, I.; Rudich, Y. Absorbing Aerosols at High Relative Humidity:
640 Linking Hygroscopic Growth to Optical Properties. *Atmos. Chem. Phys.* **2012**, *12* (12),
641 5511–5521.
- 642 (13) Lang-Yona, N.; Rudich, Y.; Segre, E.; Dinar, E.; Abo-Riziq, A. Complex Refractive
643 Indices of Aerosols Retrieved by Continuous Wave-Cavity Ring Down Aerosol
644 Spectrometer. *Anal. Chem.* **2009**, *81*, 1762–1769.
- 645 (14) Flores, J. M.; Washenfelder, R. A.; Adler, G.; Lee, H. J.; Segev, L.; Laskin, J.; Laskin, A.;
646 Nizkorodov, S. A.; Brown, S. S.; Rudich, Y. Complex Refractive Indices in the near-
647 Ultraviolet Spectral Region of Biogenic Secondary Organic Aerosol Aged with Ammonia.
648 *Phys. Chem. Chem. Phys.* **2014**, *16* (22), 10629–10642.
- 649 (15) Singh, S.; Fiddler, M. N.; Smith, D.; Bililign, S. Error Analysis and Uncertainty in the
650 Determination of Aerosol Optical Properties Using Cavity Ring-down Spectroscopy,

- 651 Integrating Nephelometry, and the Extinction-Minus-Scattering Method. *Aerosol Sci.*
652 *Technol.* **2014**, *48* (12), 1345–1359.
- 653 (16) Toole, J. R.; Renbaum-Wolff, L.; Smith, G. D. A Calibration Technique for Improving
654 Refractive Index Retrieval from Aerosol Cavity Ring-Down Spectroscopy A Calibration
655 Technique for Improving Refractive Index Retrieval from Aerosol Cavity Ring-Down
656 Spectroscopy. **2013**, 6826.
- 657 (17) Miles, R. E. H.; Rudic, S.; Orr-Ewing, A. J.; Reid, J. P. Influence of Uncertainties in the
658 Diameter and Refractive Index of Calibration Polystyrene Beads on the Retrieval of
659 Aerosol Optical Properties Using Cavity Ring Down Spectroscopy. **2010**, *114*, 7077–
660 7084.
- 661 (18) Lack, D. A.; Lovejoy, E. R.; Baynard, T.; Pettersson, A.; Ravishankara, A. R. Aerosol
662 Absorption Measurement Using Photoacoustic Spectroscopy: Sensitivity, Calibration, and
663 Uncertainty Developments. *Aerosol Sci. Technol.* **2006**, *40* (9), 697–708.
- 664 (19) Zhao, W.; Xu, X.; Dong, M.; Chen, W.; Gu, X.; Hu, C.; Huang, Y.; Gao, X.; Huang, W.;
665 Zhang, W. Development of a Cavity-Enhanced Aerosol Albedometer. *Atmos. Meas. Tech.*
666 **2014**, *7* (8), 2551–2566.
- 667 (20) Onasch, T. B.; Massoli, P.; Keabian, P. L.; Hills, F. B.; Bacon, F. W.; Freedman, A.
668 Single Scattering Albedo Monitor for Airborne Particulates. *Aerosol Sci. Technol.* **2015**,
669 *49* (September), 267–279.
- 670 (21) Li, L.; Chen, J.; Chen, H.; Yang, X.; Tang, Y.; Zhang, R. Monitoring Optical Properties of
671 Aerosols with Cavity Ringdown Spectroscopy. *J. Aerosol Sci.* **2011**, *42* (4), 277–288.
- 672 (22) Utry, N.; Ajtai, T.; Pinter, M.; Tombacz, E.; Illes, E.; Bozoki, Z.; Szabo, G. Mass-Specific
673 Optical Absorption Coefficients and Imaginary Part of the Complex Refractive Indices of
674 Mineral Dust Components Measured by a Multi-Wavelength Photoacoustic Spectrometer.
675 *Atmos. Meas. Tech.* **2015**, *8* (1), 401–410.
- 676 (23) Nakayama, T.; Sato, K.; Matsumi, Y.; Imamura, T.; Yamazaki, A.; Uchiyama, A.
677 Wavelength and NO_x Dependent Complex Refractive Index of SOAs Generated from the
678 Photooxidation of Toluene. *Atmos. Chem. Phys.* **2013**, *13* (2), 531–545.

- 679 (24) Bluvshstein, N.; Michel Flores, J.; Segev, L.; Rudich, Y. A New Approach for Retrieving
680 the UV-Vis Optical Properties of Ambient Aerosols. *Atmos. Meas. Tech.* **2016**, *9* (8),
681 3477–3490.
- 682 (25) Cai, C.; Miles, R. E. H.; Cotterell, M. I.; Marsh, A.; Rovelli, G.; Rickards, A. M. J.;
683 Zhang, Y. H.; Reid, J. P. Comparison of Methods for Predicting the Compositional
684 Dependence of the Density and Refractive Index of Organic-Aqueous Aerosols. *J. Phys.*
685 *Chem. A* **2016**, *120* (33), 6604–6617.
- 686 (26) Cremer, J. W.; Thaler, K. M.; Haisch, C.; Signorell, R. Photoacoustics of Single Laser-
687 Trapped Nanodroplets for the Direct Observation of Nanofocusing in Aerosol
688 Photokinetics. *Nat. Commun.* **2016**, *7*, 10941.1-10941.7.
- 689 (27) Nakagawa, M.; Nakayama, T.; Sasago, H.; Ueda, S.; Venables, D. S.; Matsumi, Y. Design
690 and Characterization of a Novel Single-Particle Polar Nephelometer. *Aerosol Sci. Technol.*
691 **2016**, *50* (4), 392–404.
- 692 (28) Miles, R. E. H.; Walker, J. S.; Burnham, D. R.; Reid, J. P. Retrieval of the Complex
693 Refractive Index of Aerosol Droplets from Optical Tweezers Measurements. *Phys. Chem.*
694 *Chem. Phys.* **2012**, *14* (9), 3037–3047.
- 695 (29) Cotterell, M. I.; Willoughby, R. E.; Bzdek, B. R.; Orr-Ewing, A. J.; Reid, J. P. A
696 Complete Parameterization of the Relative Humidity and Wavelength Dependence of the
697 Refractive Index of Hygroscopic Inorganic Aerosol Particles. *Atmos. Chem. Phys.*
698 *Discuss.* **2017**, No. April, 1–27.
- 699 (30) Cotterell, M. I.; Preston, T. C.; Mason, B. J.; Orr-Ewing, A. J.; Reid, J. P. Extinction
700 Cross Section Measurements for a Single Optically Trapped Particle. *Proc. SPIE* **2015**,
701 9548.
- 702 (31) Mason, B. J.; Walker, J. S.; Reid, J. P.; Orr-Ewing, A. J. Deviations from Plane-Wave Mie
703 Scattering and Precise Retrieval of Refractive Index for a Single Spherical Particle in an
704 Optical Cavity. *J. Phys. Chem. A* **2014**, 2083–2088.
- 705 (32) Walker, J. S.; Carruthers, A. E.; Orr-Ewing, A. J.; Reid, J. P. Measurements of Light
706 Extinction by Single Aerosol Particles. *J. Phys. Chem. Lett.* **2013**, *4*, 1748–1752.

- 707 (33) Preston, T. C.; Mason, B. J.; Reid, J. P.; Luckhaus, D.; Signorell, R. Size-Dependent
708 Position of a Single Aerosol Droplet in a Bessel Beam Trap. *J. Opt.* **2014**, *16* (2), 25702.
- 709 (34) Cotterell, M. I.; Mason, B. J.; Preston, T. C.; Orr-Ewing, A. J.; Reid, J. P. Optical
710 Extinction Efficiency Measurements on Fine and Accumulation Mode Aerosol Using
711 Single Particle Cavity Ring-Down Spectroscopy. *Phys. Chem. Chem. Phys.* **2015**, *17* (24),
712 15843–15856.
- 713 (35) Preston, T. C.; Reid, J. P. Angular Scattering of Light by a Homogeneous Spherical
714 Particle in a Zeroth-Order Bessel Beam and Its Relationship to Plane Wave Scattering. *J.*
715 *Opt. Soc. Am. A* **2015**, *32* (6), 1053–1062.
- 716 (36) Mason, B. J.; Cotterell, M. I.; Preston, T. C.; Orr-Ewing, A. J.; Reid, J. P. Direct
717 Measurements of the Optical Cross Sections and Refractive Indices of Individual Volatile
718 and Hygroscopic Aerosol Particles. *J. Phys. Chem. A* **2015**, *119* (22), 5701–5713.
- 719 (37) Cotterell, M. I.; Preston, T. C.; Orr-Ewing, A. J.; Reid, J. P. Assessing the Accuracy of
720 Complex Refractive Index Retrievals from Single Aerosol Particle Cavity Ring-Down
721 Spectroscopy. *Aerosol Sci. Technol.* **2016**, *50* (10), 1077–1095.
- 722 (38) Chan, C. H. Effective Absorption for Thermal Blooming due to Aerosols. *Appl. Phys.*
723 *Lett.* **1975**, *26* (11), 628–630.
- 724 (39) Lin, H.-B.; Campillo, A. J. Photothermal Aerosol Absorption Spectroscopy. *Appl. Opt.*
725 **1985**, *24* (3), 422–433.
- 726 (40) Miles, R. E. H.; Guillon, M.; Mitchem, L.; McGloin, D.; Reid, J. P. The Influence of
727 Resonant Absorption and Heating on the Equilibrium Size of Aqueous-Solute Aerosol
728 Droplets. *Phys. Chem. Chem. Phys.* **2009**, *11* (33), 7312–7317.
- 729 (41) Guillon, M.; Miles, R. E. H.; Reid, J. P.; McGloin, D. Thermo-Optical Resonance Locking
730 of an Optically Trapped Salt-Water Microdroplet. *New J. Phys.* **2009**, *11* (103041), 1–10.
- 731 (42) Clegg, S. L.; Wexler, A. S. <http://www.aim.env.uea.ac.uk/aim/model3/mod3rhw.php>
732 <http://www.aim.env.uea.ac.uk/aim/model3/mod3rhw.php> (accessed Jan 1, 2016).
- 733 (43) Clegg, S. L.; Brimblecombe, P.; Wexler, A. S. A Thermodynamic Model of the System

- 734 H⁺ -NH₄⁺ -Na⁺ -SO₄²⁻ -NO₃⁻ -Cl⁻ -H₂O at 298.15 K. *J. Phys. Chem. A* **1998**, *102*,
735 2155–2171.
- 736 (44) Hargreaves, G.; Kwamena, N. O. A.; Zhang, Y. H.; Butler, J. R.; Rushworth, S.; Clegg, S.
737 L.; Reid, J. P. Measurements of the Equilibrium Size of Supersaturated Aqueous Sodium
738 Chloride Droplets at Low Relative Humidity Using Aerosol Optical Tweezers and an
739 Electrodynamic Balance. *J. Phys. Chem. A* **2010**, *114* (4), 1806–1815.
- 740 (45) Hale, G. M.; Querry, M. R. Optical Constants of Water in the 200-Nm to 200-Mm
741 Wavelength Region. *Appl. Opt.* **1973**, *12*, 555–563.
- 742 (46) Kedenburg, S.; Vieweg, M.; Gissibl, T.; Giessen, H. Linear Refractive Index and
743 Absorption Measurements of Nonlinear Optical Liquids in the Visible and near-Infrared
744 Spectral Region. *Opt. Mater. Express* **2012**, *2* (11), 1588–1611.
- 745 (47) Toon, O. B.; Pollack, J. B.; Khare, B. N. The Optical Constants of Several Atmospheric
746 Aerosol Species: Ammonium Sulfate, Aluminum Oxide, and Sodium Chloride. *J.*
747 *Geophys. Res.* **1976**, *81* (33), 5733–5748.
- 748 (48) Toon, O. B.; Pollack, J. B.; Khare, B. N. The Optical Constants of Several Atmospheric
749 Aerosol Species: Ammonium Sulfate, Aluminum Oxide, and Sodium Chloride. *J.*
750 *Geophys. Res.* **1976**, *81* (33), 5733–5748.
- 751 (49) Butler, T. J. A.; Miller, J. L.; Orr-Ewing, A. J. Cavity Ring-Down Spectroscopy
752 Measurements of Single Aerosol Particle Extinction. I. The Effect of Position of a Particle
753 within the Laser Beam on Extinction. *J. Chem. Phys.* **2007**, *126* (17), 174302:1-174302:7.
- 754 (50) Miller, J. L.; Orr-Ewing, A. J. Cavity Ring-down Spectroscopy Measurement of Single
755 Aerosol Particle Extinction. II. Extinction of Light by an Aerosol Particle in an Optical
756 Cavity Excited by a Cw Laser. *J. Chem. Phys.* **2007**, *126* (17), 174303.1-174303.7.
- 757 (51) Davies, J. F.; Miles, R. E. H.; Haddrell, A. E.; Reid, J. P. Temperature Dependence of the
758 Vapor Pressure and Evaporation Coefficient of Supercooled Water. *J. Geophys. Res.*
759 **2014**, *119* (18), 10.931-10.940.
- 760 (52) Miles, R. E. H.; Reid, J. P.; Riipinen, I. Comparison of Approaches for Measuring the
761 Mass Accommodation Coefficient for the Condensation of Water and Sensitivities to

762 Uncertainties in Thermophysical Properties. *J. Phys. Chem. A* **2012**, *116* (44), 10810–
763 10825.

764 (53) Langridge, J. M.; Richardson, M. S.; Lack, D. A.; Brock, C. A.; Murphy, D. M.
765 Limitations of the Photoacoustic Technique for Aerosol Absorption Measurement at High
766 Relative Humidity. *Aerosol Sci. Technol.* **2013**, *47* (11), 1163–1173.

767

768

